WILEY-VCH

RESEARCH ARTICLE

High-Entropy Electrolytes with High Disordered Solvation Structures for Ultra-Stable Zinc Metal Anodes

Haoran Wang,[#[a,c]] Shenzhen Deng,[#[b]] Shuai Wang,*[a,b] Wulong Li,[a] Shixing Yuan,[a] Jing Han,[b] Hongyan Fu,[c] Bingang Xu,*[b] and Lei Wei*[a]

[a] H. R. Wang, S. Wang, W. L. Li, S. X. Yuan, Prof. L. Wei
School of Electrical and Electronic Engineering, Nanyang Technological University, Singapore 639798, Singapore
E-mail: wei.lei@ntu.edu.sg

[b] S. Z. Deng, S. Wang, J. Han, Prof. B. G. Xu
Nanotechnology Center, Research Institute for Intelligent Wearable Systems, The Hong Kong Polytechnic University, Hung Hom, Kowloon, Hong Kong 999077, China.
E-mail: shuai66.wang@polyu.edu.hk;tcxubg@polyu.edu.hk

[c] H. R. Wang, Prof. H. Y. Fu
School of Electronic Science and Engineering (National Model Microelectronics College), Xiamen University, Xiamen 361005, China.
#These authors contributed equally to this work.

Supporting information for this article is given via a link at the end of the document.

Abstract: Aqueous zinc-ion batteries (ZIBs) are playing an increasingly important role in the field of energy storage owing to their low cost, high safety, and environmental friendliness. However, their practical applications are still handicapped by severe dendrite formation and side reactions (e.g., hydrogen evolution reaction and corrosion) on the zinc anodes. Herein, a low-concentration high-entropy (HE) electrolyte strategy is proposed to achieve high reversibility and ultra-durable zinc metal anode. Specifically, this HE electrolyte features multiple anions participating in coordination and highly disordered solvation shells, which would disrupt the intrinsic H-bond network between water molecules and suppress interfacial side reactions. Moreover, these diversified weakly solvated structures can lower the solvation energy of Zn^{2+} solvation configurations and enhance zinc ion diffusion kinetics, thereby promoting uniform Zn deposition and electrode interface stability. Consequently, Zn||Zn symmetric cells exhibit over 2,000 hours of cycling stability, and Zn||Cu asymmetric cells achieve a high average Coulombic efficiency of 99.9% over 500 cycles. Furthermore, the Zn||PANI full cell with the optimized HE-50mM electrolyte delivers a high specific capacity of 110.7 mAh g^{-1} over 2,000 cycles at 0.5 A g^{-1} and a capacity retention of 70.4% at 15 A g^{-1} after 10,000 cycles. Remarkably, even at a low temperature of -20 °C, the Zn||PANI full cells equipped with HE-50mM electrolyte still demonstrate long-term cycling stability over 600 cycles with a high-capacity retention of 93.5%. This research provides a promising strategy for the design of aqueous electrolytes, aiding in the development of low-cost, high-safety, and high-performance aqueous batteries.

Introduction

The demand for safety and environmental-benign of energy storage devices has increased significantly with the rapid development of electronics, wearable devices, and new energy industries.[1] Aqueous zinc-ion batteries (ZIBs) offer a promising solution for the sustainable, large-scale application of energy storage technologies owing to their low cost, high specific capacity (820 mAh g^{-1}), environmental friendliness, and intrinsic safety.[2–4] However, dendrite growth, corrosion, and hydrogen evolution reaction (HER) on the Zn anode surface severely affect the electrochemical performance (e.g., low Coulombic efficiency (CE) and lifespan) and safety (e.g., battery swelling and short-circuiting) of aqueous ZIBs, which hinders their commercialization.[5–7] To address the above issues, various strategies have been attempted, including the construction of artificial interface layers,[8–10] the design of Zn anode structures,[11–13] and the optimization of electrolyte compositions.[14–16] The optimization of electrolytes, owing to their operational flexibility and multifunctionality, could effectively regulate the solvation configuration of Zn^{2+}, thereby serving as the most cost-effective and straightforward solution for enhancing the performance of aqueous ZIBs. Essentially, the solvation/de-solvation process of Zn^{2+} plays a crucial role in the electrochemical reactions at the electrode/electrolyte interface. The solvated Zn^{2+}, forming hydrated $[Zn(H_2O)_x]^{2+}$ ion complexes in the aqueous electrolyte system, along with free water outside the Zn^{2+} solvation shell, are the primary contributors to interfacial side reactions.[17,18] Besides, owing to the strong coordination between Zn^{2+} and solvated H_2O, the de-solvation kinetics of Zn^{2+} are notably sluggish, which would exacerbate the growth of dendrites.[19] To optimize the electrolytes and improve the solvation/de-solvation process of Zn^{2+}, a variety of strategies have been proposed, which include gel electrolytes,[20,21] "water-in-salt" electrolytes,[22,23] and electrolyte additives.[24,25] However, these electrolytes would reduce the ion conductivity and increase the costs.

High-entropy (HE) materials possess appealing ideal properties and have garnered widespread attention in the energy storage field.[26–29] Inspired by the HE materials, liquid electrolytes based on an HE strategy have emerged as a new research direction.[30–32] Compared with traditional electrolytes, their more complex and diverse solvation structures have been proven to improve battery performance, as demonstrated in lithium battery systems.[33–35] Moreover, the anti-freezing property of HE electrolytes has also been demonstrated in aqueous batteries.[36–40] More importantly, by incorporating multiple salts into the solvent, the unique microstructure of HE electrolytes would exhibit greater configurational entropy, which is an effective strategy for reducing Gibbs free energy and enhancing the ion diffusion rate of electrolytes.[41] However, the contribution of HE electrolytes for

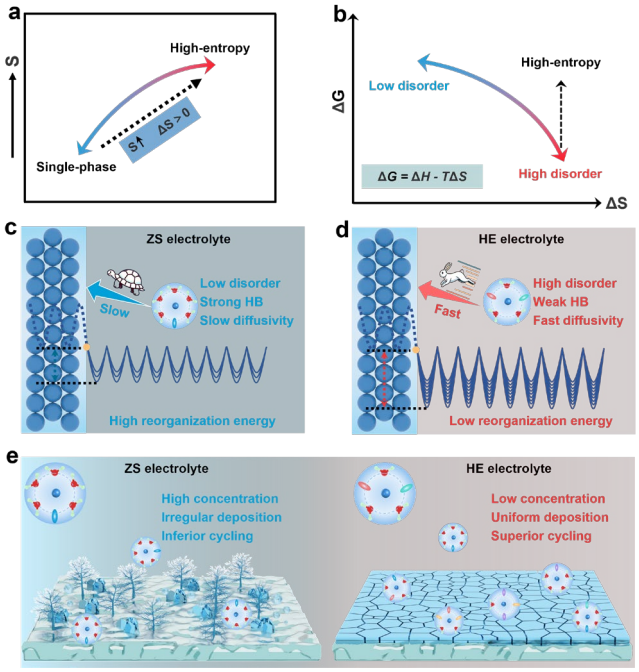

Figure 1. Schematic illustration of the design concept for an HE electrolyte. (a,b) Design concept of improving solvation entropy. ΔG, ΔH, T, and ΔS represent Gibbs free energy, enthalpy, temperature, and entropy, respectively. Zn^{2+} transport mechanism of the (c) ZS and (d) HE electrolytes. (e) Schematic diagram of the Zn anodes in the ZS and HE electrolytes.

stabilizing the Zn anode has seldom been discussed in aqueous ZIBs. The mechanism of HE electrolytes for improving electrode interface stability needs to be further studied.

Herein, we develop a low-concentration HE electrolyte by introducing five zinc salt components into an aqueous solvent to regulate the solvation structure of hydrated Zn^{2+}. Molecular dynamics (MD) simulations and spectroscopy results confirm that the number of activated water molecules around hydrated Zn^{2+} decreases in this weakly solvated electrolyte owning to multiple anions participating in coordination, which would eliminate undesirable side reactions mediated by solvated H_2O on the Zn anode. Moreover, this HE electrolyte exhibits high disorder and low solvation energy, which can accelerate the diffusion kinetics of Zn^{2+} and promote uniform Zn deposition on the Zn anode. Therefore, the proposed HE-50mM electrolyte endows Zn||Zn symmetric cells with remarkable cyclic stability (over 2,000 hours at 3 mA cm^{-2}). More importantly, the corresponding full cells exhibit superior cycling performance and rate capability at low temperature of -20 °C.

Results and Discussion

The Design Concept for an HE Electrolyte

Gibbs free energy (Δ*G*) quantifies the thermodynamic characteristics of liquid electrolyte systems. It is determined by the combination of enthalpy (Δ*H*), temperature (*T*), and solvation entropy (Δ*S*) of the system (Figure 1a, b).[34] Increasing the entropy of solvation molecules can reduce the Gibbs free energy, which is beneficial for enhancing the chemical stability and ion diffusion rate of electrolytes.[41] In addition, based on the Hofmeister effect, the anions located at the end of the Hofmeister series can effectively disrupt hydrogen bonding in water.[42] Therefore, in this work, five zinc salts with different anions ($ZnSO_4{\cdot}7H_2O$, $Zn(Ac)_2{\cdot}2H_2O$, $Zn(OTf)_2$, $Zn(ClO_4)_2{\cdot}6H_2O$, and $Zn(BF_4)_2{\cdot}4H_2O$) have been selected to construct HE electrolytes for aqueous ZIBs. By integrating diverse salts into the solvent, liquid electrolytes exhibit greater configurational entropy, thereby achieving lower Gibbs free energy. Compared with single-salt electrolytes, HE electrolytes with more complex and diverse solvation structures induce lower solvation reorganization energy, which helps to enhance the reaction kinetics of zinc ion (Figure 1c, d). Therefore, this electrolyte employing the HE strategy can effectively stabilize the zinc anode and improve the overall performance of the aqueous ZIBs (Figure 1e).

Electrolyte Structures and H-Bond Characterizations

Electrolytes with different concentrations (10mM, 50mM, 0.2M, and 0.8M) were prepared and labeled as HE-10mM, HE-50mM, HE-0.2M, and HE-0.8M electrolytes, respectively. The HE electrolytes remain transparent and stable within the concentration range of 10mM to 0.8M (Figure S1). However, at a concentration of 1M, zinc salt precipitation and recrystallization are observed. The pH values of the HE electrolytes decrease progressively from 5.62 to 3.68 as the concentration increases (Figure S2). In addition, as the concentration of HE electrolytes increases, their ionic conductivity rises, reaching an impressive

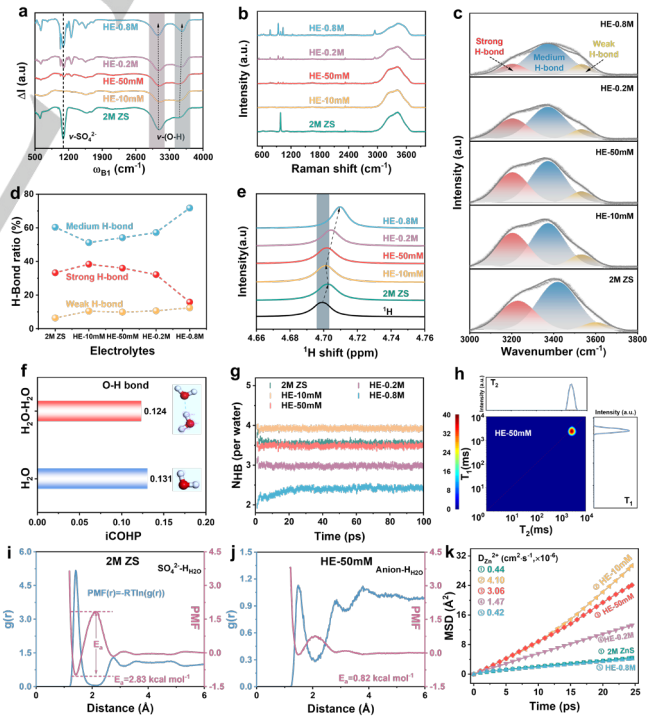

Figure 2. Electrolyte structures and H-bond characterizations. (a) FTIR spectra. (b) Raman spectra. (c) Fitted Raman spectra and (d) the proportions of strong, mediate, and weak H-bond. (e) ^1H NMR spectra. (f) The iCOHP values of O-H bonds in H_2O and H_2O-H_2O molecules. (g) The average HB number of water clusters collected from MD simulations. (h) 2D LF-NMR T_1-T_2 relaxation spectrum of the HE-50mM electrolyte. RDFs and PMFs of anion-H atom pairs in the (i) 2M ZS and (j) HE-50mM electrolytes. (k) The self-diffusion coefficient of Zn^{2+} from the mean squared displacement simulated by the MD simulations.

70.9 mS cm^{-1} at 0.8M (Figure S3). This high ionic conductivity allows the electrolyte to move more rapidly during the reaction process, significantly affecting the overall battery performance. The electrolyte structural conversion and H-bond interaction at various concentrations can be reflected by the Fourier transform infrared (FTIR) spectroscopy (Figure 2a). The O-H stretching vibration band (3,000~3,800 cm^{-1}) shifts to higher wavenumbers as the concentration of HE electrolyte increases, indicating that the complex solvation structures of HE electrolytes disrupt the intrinsic H-bond network between water molecules,[43] which is profit for suppressing the HER of activated water. Raman spectra can also provide molecular vibrational information and reflect the H-bond network on HE electrolytes at various concentrations (Figure 2b, c). The peak of O-H stretching vibration in the wavenumber range of 3,000 to 3,800 cm^{-1} can be divided into three characteristic peaks, corresponding to strong, medium, and weak H-bonds.[44] The detailed proportions of different H-bonds are plotted in Figure 2d. Compared with zinc sulfate, the ultra-low ion concentration of HE-10mM leads to enhanced hydrogen bonding interactions. As HE electrolyte concentration increases, the proportion of strong H-bonds tends to decrease, and the proportion of medium H-bonds gradually increases, indicating that HE electrolytes can disrupt the H-bond network of water in aqueous solution, which can also be confirmed by the ^1H nuclear magnetic resonance (NMR) spectra (Figure 2e).[45]

To theoretically validate our proposed mechanism, an analysis of the Crystal Orbital Hamilton Population (COHP) was conducted to reveal the effects of H-bonds on water molecules (Figure 2f and Figure S4). The strength of the O-H bond (0.12 eV/bond) in H_2O-H_2O is lower than that of the O-H bond (0.13 eV/bond) in a single H_2O molecule, which suggests that the formation of H-bonds between water molecules reduces their stability, making them more susceptible to HER. To further analyze the impact of diverse anions in HE electrolytes on the structure of water in aqueous solution, the MD simulations were conducted to statistic the average number of HB in different electrolytes (Figure 2g and Figure S5). The results demonstrate that higher concentrations of the HE electrolyte hinder the formation of a continuous H-bond network, thereby reducing the number of H-bonds in water. This observation is consistent with the FTIR and Raman spectroscopy results. Linear sweep voltammetry (LSV) tests also confirm the role of HE electrolytes in suppressing the electrochemical reduction of water (Figure S6). The above results confirm the significant role of the proposed HE electrolyte strategy in disrupting H-bonds between water molecules and suppressing interfacial side reactions.

To reveal the relationship between HE electrolytes and the dynamics of water molecules, the 2D low-field nuclear magnetic resonance (LF-NMR) spectra provide the information on the relaxation dynamics of water molecules (Figure 2h and Figure S7).[46,47]It is noteworthy that in the HE electrolytes, the T_2 of free water is greater than that observed in the ZS electrolyte, indicating a faster relaxation process of water molecules. This suggests that HE electrolytes facilitate the free movement of water molecules, aligning with the simulation results. The normalized dipole autocorrelation functions for water molecules further verify the impact of HE electrolytes on solvent dynamics (Figure S8).[48] The trends in dipolar relaxation times indicate that HE-50mM electrolyte exhibits faster relaxation in the range of 0~15 ps, suggesting accelerated solvation dynamics in this system, which could be attributed to the disruption of the H-bond network among water molecules under high disorder conditions. Radial distribution functions (RDF) and potential of mean force (PMF) were conducted to investigate the local structure and diffusion barriers of water molecules with diverse anions in the various electrolytes (Figure 2i, j and Figure S9). The RDF of SO_4^{2-}-H_{H2O} displays a distinct peak at 1.41 Å corresponding to the first hydration shells (1HS), indicating an ordered distribution of water molecules around SO_4^{2-}. Conversely, the anion-H_{H2O} pair in the HE electrolyte shows a weaker and less pronounced peak, suggesting higher disorder within the solvation shell of the HE electrolytes. The kinetic barriers associated with water molecules in the 1HS are reflected by the PMF values calculated from RDFs. It can be observed that the PMF values of HE electrolytes decrease with decreasing concentration, and the PMF value (0.82 kcal mol^{-1}) of the HE-50mM electrolyte is significantly smaller than the case (2.83 kcal mol^{-1}) of 2M ZS electrolyte. The relatively weak interaction between the diverse anions and water molecules in the HE electrolytes accelerates the kinetics of water molecules and induces a higher disordered distribution. Moreover, MD simulations were conducted to evaluate the impact of HE strategies on the kinetics of Zn^{2+}. The self-diffusion coefficient of Zn^{2+}, as derived from the mean square displacement (MSD) curves, is calculated to be 1.22×10^{-6} cm^2 s^{-1} in the HE-50mM electrolyte, which is greater than that in the 2M ZS electrolyte (Figure 2k). The activation energy (E_a) recorded from Zn||Zn symmetric cell further proves this result (Figure S10). The E_a of 39.1 kJ mol^{-1} in the HE-50mM electrolyte is significantly lower than that (70.6 kJ mol^{-1}) in the 2M ZS electrolyte, which is beneficial to ion transfer kinetics. These results demonstrate that HE electrolytes can facilitate the migration and macroscopically uniform deposition of Zn^{2+}.[49]

High Disordered Solvation Structures

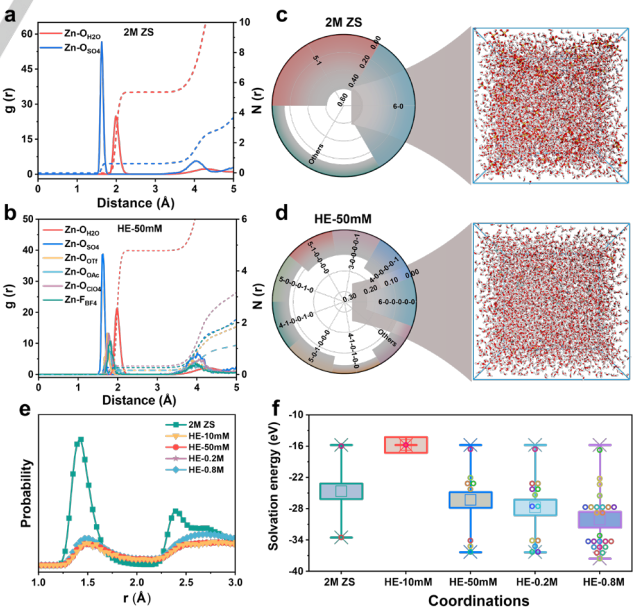

Figure 3. High disordered solvation structures. The RDFs of cation-(anion and H_2O) and the radius-dependent coordination numbers in the (a) 2M ZS and (b) HE-50mM electrolytes. Zn^{2+} coordination environments of the (c) 2M ZS and (d) HE-50mM electrolytes calculated from MD simulations. (e) Distribution of the distance and probability between the anion and water molecules. (f) The solvation energy of Zn^{2+} solvation configurations in the various electrolytes.

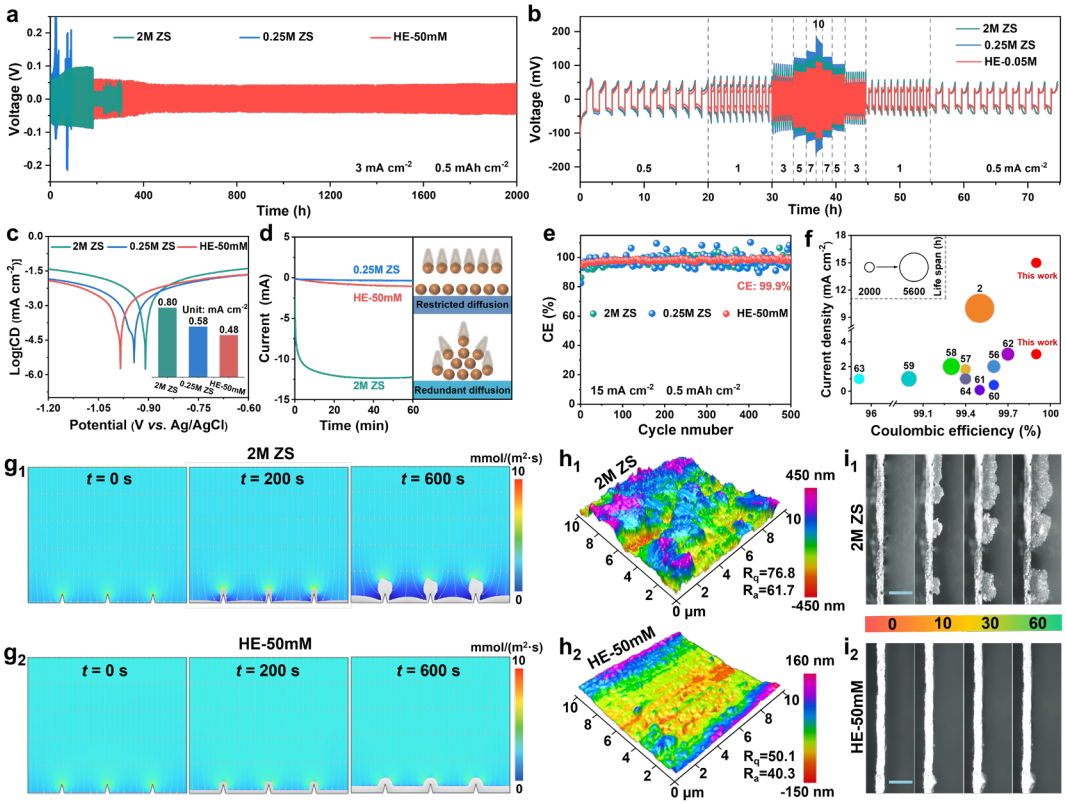

Figure 4. Zn plating/stripping behaviors in the various electrolytes. (a) Cycling performance of Zn||Zn symmetric cells tested at 3 mA cm^{-2}, 0.5 mAh cm^{-2}. (b) The rate performances of Zn||Zn symmetric cells at 0.5-10 mA cm^{-2}. (c) Tafel curves and the corresponding corrosive current densities. (d) CA of Zn||Zn cells at -150 mV overpotential. (e) CE of the Zn||Cu cells at 15 mA cm^{-2}, 0.5 mAh cm^{-2}. (f) Comparison with the previous literatures. Electric field and concentration field simulation in the (g_1) 2M ZS and (g_2) HE-50mM electrolytes. AFM images of cycled Zn anodes in the (h_1) 2M ZS and (h_2) HE-50mM electrolytes. R_a means average roughness and R_q means root-mean-square roughness. *In-situ* optical microscopy images of the Zn plating process in the (i_1) 2M ZS and (i_2) HE-50mM electrolytes, scale bar: 100 μm.

Density functional theory (DFT) calculations and MD simulations were conducted to obtain RDF and coordination distribution functions, providing insight into the potential mechanisms by which HE electrolytes influence the solvation structure of Zn^{2+} (Figure 3a, b, and Figure S11 and Table S1). In the 2M ZS electrolyte, Zn^{2+} typically coordinates with five H_2O and one SO_4^{2-}. A sharp peak at approximately 2.1 Å indicates a structured arrangement of H_2O around Zn^{2+} ions within the solvation shells. In addition, unlike the typical solvation structures of $Zn[H_2O]_6^{2+}$ and $Zn^{2+}[H_2O]_5[SO_4^{2-}]$ that dominate the solvation environment in the 2M ZS electrolyte, more anions are involved in the solvation shells in HE electrolytes. The various major anion species in the HE-0.8M electrolyte contribute to the rich diversity of the Zn^{2+} solvation shells, resulting in a more complex and diverse solvation structure, along with a reduced proportion of typical solvation structures. (Figure 3c, d, and Figures S12-S19 and Tables S2-S7). Although the diversity of solvation structures in the HE systems decreases with the reduction in electrolyte concentration, the diversity of the solvation structures far exceeds that in the 2M ZS electrolyte even at a low concentration such as HE-50mM, enhancing the disorderliness of the electrolyte. The distribution of the distance between the anion and H_2O was calculated to further explore the degree of disorder in different electrolytes (Figure 3e). In the 2M ZS electrolyte, the distribution features a distinct sharp peak, suggesting a more ordered solvation environment. However, in the HE electrolytes, the distribution lacks sharp peaks, and the distances between the anions and H_2O show a more uniform distribution, which indicates a higher degree of disorder. The significant difference in the degree of disorder between the 2M ZS and HE electrolytes is consistent with the diversity of Zn^{2+} coordination environments.

To further reveal the advantage of HE electrolytes, the interactions between the anions and H_2O/Zn^{2+} were analyzed using DFT calculations. As shown in the electrostatic potential (ESP) mappings (Figure S20), all the anions, including OTf^-, Ac^-, ClO_4^-, BF_4^- and SO_4^{2-}, show higher local electronegativity than H_2O, which facilitates their preferential coordination with Zn^{2+} within the solvation shell, thereby promoting hydrogen bond disruption. Moreover, the binding energy of Zn^{2+} with various anions is significantly lower than that of Zn-H_2O (Figure S21), indicating that the solvation structure is stable in HE systems and that Zn^{2+} prefers binding with anions over H_2O.[50,51] Additionally, DFT calculations revealed the impact of HE electrolyte systems on solvation energy (Figure 3f). In HE electrolytes from HE-50mM to HE-0.8M, the solvation energies are lower than that in the ZS electrolyte. Moreover, as the concentration increases, the energy of the solvation structure decreases gradually, which could be attributed to the diverse and complex solvation structures in HE electrolytes. The diverse and highly disordered solvation structures reduce the diffusion barrier during the nucleation stage and enhance the kinetics of Zn^{2+} (Figure S10 and Figure 2k), favoring a reduction in the nucleation overpotential of Zn deposition and promoting nucleation with a uniform deposition morphology.

Zn Plating/Stripping Behaviors in the Various Electrolytes

The Zn‖Zn symmetric cells were assembled to assess the Zn plating/stripping behaviors in the various electrolytes. The cells with HE electrolytes exhibit better cycling durability than those with the ZS electrolyte (Figures S22 and S23). Typically, the symmetric cells using HE-50mM, HE-0.2mM, and HE-0.8mM electrolytes display a long-term cycling life (over 2,000 h) and a low overpotential (below 50 mV) at 0.5 mA cm^{-2}. Owing to the diminished ionic conductivity of the ultra-low zinc salt concentration (Figure S3), the Zn‖Zn symmetric cell with HE-10mM electrolyte exhibits an unsatisfactory cycling life. Moreover, excessively high-concentration zinc salts would heighten the viscosity, cost, and corrosiveness of the electrolytes. Impressively, the HE-50 mM electrolyte with a low salt concentration can not only help to suppress water-induced side reactions and stabilize aqueous electrolytes, but also have low-cost advantages. Thus, the optimal concentration for HE electrolytes is determined to be 50 mM, and subsequent research in this work focuses on the HE-50 mM electrolyte. The Zn||Zn symmetric cells with HE-50mM electrolyte still cycle for over 2,000 hours even at a high current density of 3 mA cm^{-2}, significantly outperforming that with the single-salt ZS electrolytes (Figure 4a). The inferior electrochemical performance of the 0.25M single salt ZS electrolyte, at the same concentration as the HE-50mM electrolyte, validates further the effectiveness of the low-concentration HE electrolyte strategy. Moreover, the symmetric cells with HE-50mM electrolyte exhibit a superior rate capability (Figure 4b and Figure S24). As the current density increases from 0.5 to 10.0 mA cm^{-2}, symmetric cells with HE-50mM electrolyte consistently exhibit smaller voltage hysteresis compared to the cells with the single-salt ZS electrolytes. Remarkably, the HE-50mM electrolyte delievers excellent performance even at low temperatures owing to its diverse and highly disordered solvation shell (Figure S25). When the temperature drops to -20 °C, the Zn||Zn symmetric cell with HE-50mM electrolyte can still cycle stably for over 300 hours at 3 mA cm^{-2} with an areal capacity of 0.5 mAh cm^{-2}. Furthermore, the calculated corrosion currents for the Zn anode in the HE-50mM electrolyte is 0.48 mA cm^{-2}, which is lower than that of 0.8 and 0.58 mA cm^{-2} in the 2M and 0.25 M ZS electrolytes (Figure 4c), suggesting better corrosion resistance of the Zn anode in the HE-50mM electrolyte.[52] In addition, an immersion experiment was conducted to further investigate the corrosion behavior of the Zn anodes in the various electrolytes (Figure S26). After immersing zinc metal in the HE-50mM electrolyte for 7 days, scarcely any by-products and corrosion marks were observed on the surface of the Zn electrode, indicating its superior corrosion resistance. However, the zinc metals were corroded severely in the 2M ZS and 0.25M ZS electrolytes. In order to evaluate the impact of multiple anions on the electrode's electric double layer (EDL) structure, the EDL capacitance was investigated through the cyclic voltammetry (CV) curves of the Zn||Zn cell (Figure S27). The Zn||Zn cell exhibits a lower EDL capacitance in the HE-50mM electrolyte (0.353 mF cm^{-2}) than that in the 2M ZS and 0.25M ZS electrolytes, suggesting that partial anions enter into the inner Helmholtz plane of the EDL in the HE-50mM electrolyte, thus establishing a water-poor EDL,[53] which is profit to suppress HER and side reactions on the zinc anode.[54]

To investigate the nucleation mechanism of the zinc deposition process, chronoamperometry (CA) measurements were conducted on a symmetric cell with an overpotential of -150 mV (Figure 4d). In the 2M ZS electrolyte, the current rapidly increases (in absolute value) for over 120 s and continues to rise beyond 300 s. This indicates that a rapid and uncontrolled two-dimensional diffusion occurs on the zinc anode, leading to uneven deposition and a rapid increase in specific surface area.[55] In contrast, the highly disordered HE-50mM electrolyte delivers a consistent 3D diffusion after a shorter nucleation stage, which is profitable to improve the diffusion process and promote uniform deposition of the zinc layer. In addition, in the 0.25M ZS electrolyte, the absolute deposition current density remained always quite small during the entire process, which could be attributed to that the low ionic conductivity hinders the reduction mechanism. Moreover, the CE of Zn||Cu cells was tested to investigate the reversibility of Zn anodes in the various electrolytes (Figure 4e, and Figures S28 and S29). The average CE in the ZS electrolytes exhibits significant fluctuations, indicating poor reversibility due to severe dendritic growth and side reactions. By contrast, the cell with the HE-50mM electrolyte displays a stable CE of ~ 99.9% (15 mA cm^{-2}, 0.5 mAh cm^{-2} and 3 mA cm^{-2}, 1 mAh cm^{-2}) over hundreds of cycles, showcasing the high reversibility of the Zn plating/stripping process. Notably, compared with previously reported studies,[2,56–64] the cell with the HE-50mM electrolyte displays competitive advantages in terms of CE and span life (Figure 4f and Table S8), paving a good way for practical aqueous batteries.

The effect of HE-50mM electrolyte on suppressing the dendritic growth of the Zn anode was also investigated by Finite Element Modeling (FEM) (Figure 4g_1-g_2 and Figure S30). In the ZS electrolyte, as the deposition process advances, zinc predominantly accumulates around the tips because of the inferior Zn^{2+} diffusion kinetics, thereby exacerbating the growth of zinc dendrites.[65,66] However, the HE-50mM electrolyte with high disorder can enhance the Zn^{2+} diffusion and endow the Zn anode surface with a more even distribution of Zn^{2+} ions flux, thus promoting uniform zinc deposition. The adsorption energy results of solvation structures on different Zn planes confirm that the solvation structures in the HE electrolytes exhibit a higher adsorption affinity for the Zn(002) plane (Figure S31), indicating that high disordered solvation structures can guide the uniform Zn depositon along with the Zn(002) plane, which can also be confirmed by the wide-angle X-ray scattering (WAXS) and X-ray diffraction (XRD) patterns (Figures S32 and S33). Compared with pure Zn anode and other electrolytes, the intensity of the Zn(002) plane in the HE-50 mM electrolyte is more concentrated and uniform, and a higher value (0.91) of I_{002}/I_{101} is obtained, which suggests that zinc deposition exhibits a preferential growth orientation along the Zn(002) plane, thereby suppressing the formation of Zn dendrites.[67] Scanning electron microscopy (SEM) and atomic force microscopy (AFM) were carried out to further verify the inhibition of dendritic growth on the Zn anode surface. There are no significant dendritic formations on the Zn surface in the HE-50mM electrolyte since the nucleation sites for Zn^{2+} are uniformly distributed (Figure S34). However, the Zn anodes are covered with large petal-like products in the ZS electrolytes. The roughness values (R_q = 50.1 nm, R_a = 40.3 nm) of deposited Zn in the HE-50mM electrolyte are significantly smaller than those (R_q = 76.8 nm, R_a = 67.1 nm) in the ZS electrolytes (Figure 4h_1-h_2 and Figure S35). The difference of Zn plating between HE-50mM and ZS electrolytes is also identified via the *in-situ* optical microscopy images (Figure 4i_1-i_2 and Figure

S36). In the HE-50mM electrolyte, the Zn anode displays a smooth, dendrite-free surface during the plating process. By contrast, some small protrusions emerge on the Zn anode and gradually evolve into Zn dendrites in the ZS electrolytes.

Electrochemical Performance of Zn||PANI Cells and Soft-Packaged Zn||MnO_2 Cells

The practicality of the HE-50mM electrolyte can be validated by the Zn||PANI full cells, where PANI and Zn are used as the cathode and anode, respectively (Figure S37). The full cell with the HE-50mM electrolyte exhibits higher specific capacities than that with the ZS electrolytes under the various current densities (Figure 5a and Figure S38). At a low current density of 0.2 A g^{-1}, the specific capacities of the full cell with 2M ZS, 0.25M ZS, and HE-50 mM electrolytes are 109.6, 67.3, and 166.0 mAh g^{-1}, respectively. When the current density increases to 5.0 A g^{-1}, the full cell with the HE-50 mM electrolyte still maintains a high specific capacity of 72.7 mAh g^{-1}. When the current density returns to 0.2 A g^{-1}, the full cell based on HE-50mM electrolyte shows good capacity retention. The excellent rate capability could be attributed to the fast Zn^{2+} diffusion rate in the HE-50mM electrolyte, which indicates that the HE-50mM electrolyte with more complex and diversified weakly solvated structures can enhance the reaction kinetics of zinc ions and the reversibility of Zn^{2+}. The enhanced reaction kinetics of cells with HE-50mM electrolyte can be further demonstrated by electrochemical impedance spectroscopy (EIS), galvanostatic intermittent titration technique (GITT), and CV curves (Figure 5b, and Figures S39 and S40). For instance, the charge transfer resistance of the Zn||PANI full cell in the HE-50mM electrolyte is much lower than that in the ZS electrolytes after 10 cycles. The GITT measurements indicate that the Zn^{2+} diffusion coefficient in the HE electrolyte is an order of magnitude higher than that in the 2M ZS and 0.25M ZS electrolytes. In the CV curves, the current density and potential of the cathodic peak B increase in the HE-50mM electrolyte. To investigate the stability of full cells using HE-50mM electrolyte, long-term cycling performance tests were conducted on both Zn||PANI full cells and Zn-I_2 full cells. The Zn||PANI full cell with the HE-50mM electrolyte still delivers a high capacity of 110.7 mAh g^{-1} over 2,000 cycles (Figure 5c), which is markedly better than in the cases of the ZS electrolytes. Even at a high current density of 15.0 A g^{-1}, the full cell with the HE-50mM electrolyte maintains 70.4% of its initial capacity over 10,000 cycles (Figure S41). The enhanced electrochemical performance of Zn||PANI full cells with the HE-50mM electrolyte is also testified by the self-discharge tests (Figure 5d and Figure S42). Impressively, even at a low temperature of -20 °C, the Zn||PANI full cells with HE-50mM electrolyte exhibit long-term stability over 600 cycles with a high-capacity retention of 93.5% and superior rate capability (Figure 5e-g). In addition, to verify the feasibility of the practical applications, a Zn−I_2 full cell with high mass loading was assembled and its electrochemical performance was evaluated (Figure S43). The Zn−I_2 full cell with the HE-50mM electrolyte delivers a high capacity of 111.4 mAh g^{-1} after 2,000 cycles, with a capacity retention of 83.9%, suggesting its excellent cycling stability in the HE-50mM electrolyte.

Lastly, Zn||MnO_2 pouch cells were also assembled to illustrate further the feasibility of practical applications of the HE-50mM electrolyte (Figure 5h, and Figures S44 and S45). Each

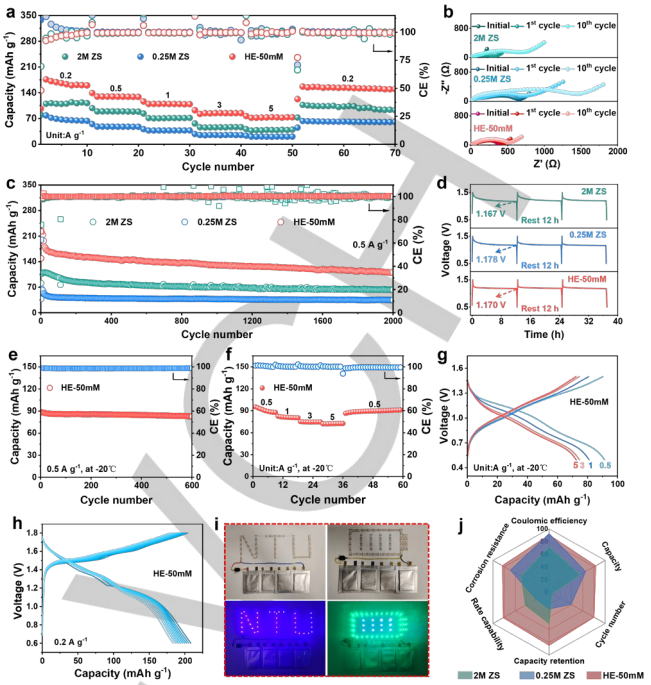

Figure 5. Electrochemical performance of Zn||PANI cells and soft-packaged Zn||MnO_2 cells. (a) Rate capability. (b) EIS measurements. (c) Cycling performance at 0.5 A g^{-1} over 2000 cycles. (d) Self-discharge tests of Zn||PANI cells. (e) The cycling performance (0.5 A g^{-1}) of Zn||PANI cell at -20 °C. (f) Rate capabilities and (g) the corresponding charge-discharge curves of Zn||PANI cell with the HE-50 mM electrolyte at -20 °C. (h) The corresponding charge-discharge curves of soft-packaged Zn||MnO_2 cell. (i) Optical photos of LEDs powered by the pouch cells in series. (j) Radar chart of the performance for ZS and HE-50mM electrolytes.

pouch cell delivers an open-circuit voltage of approximately 1.5 V, and four pouch cells connected in series successfully illuminate an LED pattern (Figure 5i), demonstrating the promising application prospects of low-concentration HE electrolytes. Based on the above results, the properties of the three electrolytes are compared in the radar chart (Figure 5j). The low-concentration HE-50mM electrolyte exhibits multifunctional properties, including corrosion resistance, high CE, long-term cycling life, high-rate capability, and high-capacity retention, showing significant overall advantages over the ZS electrolytes.

Conclusion

In summary, we have developed an economical and efficient HE electrolyte with more complex and highly disordered solvation structures. This HE electrolyte can effectively suppress HER and side reactions on the zinc anode by disrupting H-bond networks, reducing solvated water activity, and optimizing Zn^{2+} solvation. Moreover, the enhanced Zn^{2+} diffusion kinetics and the low solvation energy of Zn^{2+} solvation configurations promote the rapid uniform Zn plating/stripping. As a result, Zn||Zn symmetric cells using the HE electrolyte achieve over 2,000 hours of cyclic stability at 3 mA cm^{-2}, and Zn||PANI full cells with the HE-50mM electrolyte maintain a high specific capacity of 110.7 mAh g^{-1} after 2,000 cycles. Even at a low temperature of -20 °C, the Zn||Zn symmetric and Zn||PANI full cells still demonstrate enduring durability and distinguished electrochemical performance. This

low-concentration HE-50mM electrolyte demonstrates multiple significant benefits and offers new possibilities for the design and optimization of electrolytes for other aqueous metal-based batteries.

Acknowledgements

This work was supported by the Singapore Ministry of Education Academic Research Fund Tier 2 (MOE2019-T2-2-127, MOE-T2EP50120-0002 and MOE-T2EP50123-0014), the Singapore Ministry of Education Academic Research Fund Tier 1 (RG62/22), A*STAR under AME IRG (A2083c0062), A*STAR under IAF-ICP Programme I2001E0067 and the Schaeffler Hub for Advanced Research at NTU, the IDMxS (Institute for Digital Molecular Analytics and Science) by the Singapore Ministry of Education under the Research Centres of Excellence scheme, China Scholarship Council (No. 202206310050), and the NTU-PSL Joint Lab collaboration. The authors would like to thank Shiyanjia Lab (www.shiyanjia.com) for the LF-NMR analysis.

Conflict of Interest

The authors declare no conflict of interest.

Keywords: high-entropy electrolytes • high disordered solvation shells • reaction kinetics • enhanced electrochemical performance

[1] J. Zhang, Y. Liu, Y. Wang, Z. Zhu, Z. Yang, *Adv. Funct. Mater.* **2024**, *34*, 2401889.
[2] X. Yang, W. Li, Z. Chen, M. Tian, J. Peng, J. Luo, Y. Su, Y. Zou, G. Weng, Y. Shao, S. Dou, J. Sun, *Angew. Chem. Int. Ed.* **2023**, *62*, e202218454.
[3] S. Deng, B. Xu, J. Zhao, C. W. Kan, X. Liu, *Angew. Chem. Int. Ed.* **2024**, *63*, e202401996.
[4] M. Zhong, Y. Wang, Y. Xie, S. Yuan, K. Ding, E. J. Begin, Y. Zhang, J. L. Bao, Y. Wang, *Adv. Funct. Mater.* **2024**, *34*, 2316788.
[5] H. Kang, S.-H. Kim, D. B. Ahn, X. Wang, Z.-S. Wu, S.-Y. Lee, *ACS Energy Lett.* **2024**, 2816–2825.
[6] S. Deng, Z. Tie, F. Yue, H. Cao, M. Yao, Z. Niu, *Angew. Chem. Int. Ed.* **2022**, *134*, e202115877.
[7] Y. Wang, Z. Wang, W. K. Pang, W. Lie, J. A. Yuwono, G. Liang, S. Liu, A. M. D. Angelo, J. Deng, Y. Fan, K. Davey, B. Li, Z. Guo, *Nat. Commun.* **2023**, *14*, 2720.
[8] Y. Yang, C. Liu, Z. Lv, H. Yang, Y. Zhang, M. Ye, L. Chen, J. Zhao, C. C. Li, *Adv. Mater.* **2021**, *33*, 2007388.
[9] B. Wei, J. Zheng, Abhishek, X. Liu, J. Wu, Z. Qi, Z. Hou, R. Wang, J. Ma, A. N. Gandi, Z. Wang, H. Liang, *Adv. Energy Mater.* **2024**, *14*, 2401018.
[10] C. Deng, X. Xie, J. Han, Y. Tang, J. Gao, C. Liu, X. Shi, J. Zhou, S. Liang, *Adv. Funct. Mater.* **2020**, *30*, 2000599.
[11] H. Jia, X. Jiang, Y. Wang, Y. Lam, S. Shi, G. Liu, *Adv. Energy Mater.* **2024**, *14*, 2304285.
[12] Q. Li, A. Chen, D. Wang, Y. Zhao, X. Wang, X. Jin, B. Xiong, C. Zhi, *Nat. Commun.* **2022**, *13*, 3699.
[13] S. Lian, Z. Cai, M. Yan, C. Sun, N. Chai, B. Zhang, K. Yu, M. Xu, J. Zhu, X. Pan, Y. Dai, J. Huang, B. Mai, L. Qin, W. Shi, Q. Xin, X. Chen, K. Fu, Q. An, Q. Yu, L. Zhou, W. Luo, K. Zhao, X. Wang, L. Mai, *Angew. Chem. Int. Ed.* **2024**, e202406292.
[14] R. Zhao, H. Wang, H. Du, Y. Yang, Z. Gao, L. Qie, Y. Huang, *Nat. Commun.* **2022**, *13*, 3252.
[15] Y. Lv, M. Zhao, Y. Du, Y. Kang, Y. Xiao, S. Chen, *Energy Environ. Sci.* **2022**, *15*, 4748–4760.
[16] G. Li, Z. Zhao, S. Zhang, L. Sun, M. Li, J. A. Yuwono, J. Mao, J. Hao, J. (Pimm) Vongsvivut, L. Xing, C.-X. Zhao, Z. Guo, *Nat. Commun.* **2023**, *14*, 6526.
[17] X. Zeng, K. Xie, S. Liu, S. Zhang, J. Hao, J. Liu, W. K. Pang, J. Liu, P. Rao, Q. Wang, J. Mao, Z. Guo, *Energy Environ. Sci.* **2021**, *14*, 5947–5957.
[18] T. C. Li, Y. Lim, X. L. Li, S. Luo, C. Lin, D. Fang, S. Xia, Y. Wang, H. Y. Yang, *Adv. Energy Mater.* **2022**, *12*, 2103231.
[19] S. Yang, A. Chen, Z. Tang, Z. Wu, P. Li, Y. Wang, X. Wang, X. Jin, S. Bai, C. Zhi, *Energy Environ. Sci.* **2024**, *17*, 1095–1106.
[20] Y. Wang, Q. Li, H. Hong, S. Yang, R. Zhang, X. Wang, X. Jin, B. Xiong, S. Bai, C. Zhi, *Nat. Commun.* **2023**, *14*, 3890.
[21] C. Lu, H. Jiang, X. Cheng, J. He, Y. Long, Y. Chang, X. Gong, K. Zhang, J. Li, Z. Zhu, J. Wu, J. Wang, Y. Zheng, X. Shi, L. Ye, M. Liao, X. Sun, B. Wang, P. Chen, Y. Wang, H. Peng, *Nature* **2024**, *629*, 86–91.
[22] F. Wang, O. Borodin, T. Gao, X. Fan, W. Sun, F. Han, A. Faraone, J. A. Dura, K. Xu, C. Wang, *Nat. Mater.* **2018**, *17*, 543–549.
[23] L. Ma, N. Li, C. Long, B. Dong, D. Fang, Z. Liu, Y. Zhao, X. Li, J. Fan, S. Chen, S. Zhang, C. Zhi, *Adv. Funct. Mater.* **2019**, *29*, 1906142.
[24] W. Zhang, M. Dong, K. Jiang, D. Yang, X. Tan, S. Zhai, R. Feng, N. Chen, G. King, H. Zhang, H. Zeng, H. Li, M. Antonietti, Z. Li, *Nat. Commun.* **2022**, *13*, 5348.
[25] X. Shi, J. Xie, J. Wang, S. Xie, Z. Yang, X. Lu, *Nat. Commun.* **2024**, *15*, 302.
[26] J.-W. Yeh, S.-K. Chen, S.-J. Lin, J.-Y. Gan, T.-S. Chin, T.-T. Shun, C.-H. Tsau, S.-Y. Chang, *Adv. Eng. Mater.* **2004**, *6*, 299–303.
[27] B. Cantor, I. T. H. Chang, P. Knight, A. J. B. Vincent, *Mater. Sci. Eng. A* **2004**, *375*, 213–218.
[28] Z. Liu, R. Liu, S. Xu, J. Tian, J. Li, H. Li, T. Yu, S. Chu, A. M. D'Angelo, W. K. Pang, L. Zhang, S. Guo, H. Zhou, *Angew. Chem. Int. Ed.* **2024**, *63*, e202405620.
[29] B. Wang, J. Ma, K. Wang, D. Wang, G. Xu, X. Wang, Z. Hu, C.-W. Pao, J.-L. Chen, L. Du, X. Du, G. Cui, *Adv. Energy Mater.* **2024**, *14*, 2401090.
[30] S. Chai, J. Xia, Y. Li, J. Liu, *Next Energy* **2024**, *2*, 100077.
[31] H. Zhang, Y. Wang, J. Huang, W. Li, X. Zeng, A. Jia, H. Peng, X. Zhang, W. Yang, *ENERGY Environ. Mater.* **2024**, *7*, e12514.
[32] S. Wang, K. Wang, Y. Zhang, Y. Jie, X. Li, Y. Pan, X. Gao, Q. Nian, R. Cao, Q. Li, S. Jiao, D. Xu, *Angew. Chem. Int. Ed.* **2023**, *62*, e202304411.
[33] Q. Wang, C. Zhao, J. Wang, Z. Yao, S. Wang, S. G. H. Kumar, S. Ganapathy, S. Eustace, X. Bai, B. Li, M. Wagemaker, *Nat. Commun.* **2023**, *14*, 440.
[34] Q. Wang, C. Zhao, Z. Yao, J. Wang, F. Wu, S. G. H. Kumar, S. Ganapathy, S. Eustace, X. Bai, B. Li, J. Lu, M. Wagemaker, *Adv. Mater.* **2023**, *35*, 2210677.
[35] S. C. Kim, J. Wang, R. Xu, P. Zhang, Y. Chen, Z. Huang, Y. Yang, Z. Yu, S. T. Oyakhire, W. Zhang, L. C. Greenburg, M. S. Kim, D. T. Boyle, P. Sayavong, Y. Ye, J. Qin, Z. Bao, Y. Cui, *Nat. Energy* **2023**, *8*, 814–826.
[36] C. Yang, J. Xia, C. Cui, T. P. Pollard, J. Vatamanu, A. Faraone, J. A. Dura, M. Tyagi, A. Kattan, E. Thimsen, J. Xu, W. Song, E. Hu, X. Ji, S. Hou, X. Zhang, M. S. Ding, S. Hwang, D. Su, Y. Ren, X.-Q. Yang, H. Wang, O. Borodin, C. Wang, *Nat. Sustain.* **2023**, *6*, 325–335.
[37] H. Ji, C. Xie, T. Wu, H. Wang, Z. Cai, Q. Zhang, W. Li, L. Fu, H. Li, H. Wang, *Chem. Commun.* **2023**, *59*, 8715–8718.
[38] H. Jia, X. Jiang, Y. Wang, Y. Lam, S. Shi, G. Liu, *Adv. Energy Mater.* **2024**, *14*, 2304285.
[39] M. Qiu, P. Sun, K. Han, Z. Pang, J. Du, J. Li, J. Chen, Z. L. Wang, W. Mai, *Nat. Commun.* **2023**, *14*, 601.
[40] J. Xu, *Mater. Futur.* **2023**, *2*, 047501.
[41] X. Zhao, Z. Fu, X. Zhang, X. Wang, B. Li, D. Zhou, F. Kang, *Energy Environ. Sci.* **2024**, *17*, 2406–2430.
[42] S Deng, B Xu, J Zhao, H Fu, *Energy Storage Mater.* **2024**, 70, 103490.
[43] R. Wang, M. Yao, M. Yang, J. Zhu, J. Chen, Z. Niu, *Proc. Natl. Acad. Sci.* **2023**, *120*, e2221980120.
[44] G. Duan, Y. Wang, B. Luo, L. Sun, S. Zheng, J. Huang, Z. Ye, *Energy Storage Mater.* **2023**, *61*, 102882.
[45] M. Wang, J. Ma, Y. Meng, J. Sun, Y. Yuan, M. Chuai, N. Chen, Y. Xu, X. Zheng, Z. Li, W. Chen, *Angew. Chem. Int. Ed.* **2023**, *62*, e202214966.
[46] S. Wang, R. Lin, shasha Cheng, M. Tan, *Food Chem.* **2020**, *320*, 126622.

[47] L. Chen, Y. Tian, Q. Tong, Z. Zhang, Z. Jin, *Food Chem.* **2017**, *214*, 702–709.
[48] J. C. Wilson, S. Caratzoulas, D. G. Vlachos, Y. Yan, *Nat. Commun.* **2023**, *14*, 2384.
[49] X. Xie, S. Liang, J. Gao, S. Guo, J. Guo, C. Wang, G. Xu, X. Wu, G. Chen, J. Zhou, *Energy Environ. Sci.* **2020**, *13*, 503–510.
[50] S. Huang, L. Hou, T. Li, Y. Jiao, P. Wu, *Adv. Mater.* **2022**, *34*, 2110140.
[51] N. Hu, W. Lv, W. Chen, H. Tang, X. Zhang, H. Qin, D. Huang, J. Zhu, Z. Chen, J. Xu, H. He, *Adv. Funct. Mater.* **2024**, *34*, 2311773.
[52] R. Deng, Z. He, F. Chu, J. Lei, Y. Cheng, Y. Zhou, F. Wu, *Nat. Commun.* **2023**, *14*, 4981.
[53] L. Jiang, D Li, X Xie, D Ji, L Li, L Li, Z He, B Lu, S Liang, J Zhou *Energy Storage Mater.* **2023**, 62, 102932.
[54] Z. Wang, J. Diao, G. Henkelman, C. B. Mullins, *Adv Funct Mater.* **2024**, 34, 2314002.
[55] K. Zhu, C. Guo, W. Gong, Q. Xiao, Y. Yao, K. Davey, Q. Wang, J. Mao, P. Xue, Z. Guo, *Energy Environ. Sci.* **2023**, *16*, 3612–3622.
[56] R. Sun, D. Han, C. Cui, Z. Han, X. Guo, B. Zhang, Y. Guo, Y. Liu, Z. Weng, Q.-H. Yang, *Angew. Chem. Int. Ed.* **2023**, *62*, e202303557.
[57] R. Zhao, Y. Yang, G. Liu, R. Zhu, J. Huang, Z. Chen, Z. Gao, X. Chen, L. Qie, *Adv. Funct. Mater.* **2021**, *31*, 2001867.
[58] J. Luo, L. Xu, Y. Zhou, T. Yan, Y. Shao, D. Yang, L. Zhang, Z. Xia, T. Wang, L. Zhang, T. Cheng, Y. Shao, *Angew. Chem. Int. Ed.* **2023**, *62*, e202302302.
[59] Y. Wu, T. Zhang, L. Chen, Z. Zhu, L. Cheng, S. Gu, Z. Li, Z. Tong, H. Li, Y. Li, Z. Lu, W. Zhang, C. S. Lee, *Adv. Energy Mater.* **2023**, *13*, 2300719.
[60] X. Nie, L. Miao, W. Yuan, G. Ma, S. Di, Y. Wang, S. Shen, N. Zhang, *Adv. Funct. Mater.* **2022**, *32*, 2203905.
[61] D. Han, T. Sun, R. Zhang, W. Zhang, T. Ma, H. Du, Q. Wang, D. He, S. Zheng, Z. Tao, *Adv. Funct. Mater.* **2022**, *32*, 2209065.
[62] P. Wu, L. Xu, X. Xiao, X. Ye, Y. Meng, S. Liu, *Adv. Mater.* **2024**, *36*, 2306601.
[63] H. Liu, J. Li, D. Wei, X. Liu, Z. Cai, H. Zhang, Z. Lv, L. Chen, H. Li, H. Luo, Y. Zhao, H. Yu, X. Wang, F. Chen, G. Zhang, H. Duan, *Adv. Funct. Mater.* **2023**, *33*, 2300419.
[64] L. Hong, X. Wu, Y.-S. Liu, C. Yu, Y. Liu, K. Sun, C. Shen, W. Huang, Y. Zhou, J.-S. Chen, K.-X. Wang, *Adv. Funct. Mater.* **2023**, *33*, 2300952.
[65] Z. Miao, F. Zhang, H. Zhao, M. Du, H. Li, H. Jiang, W. Li, Y. Sang, H. Liu, S. Wang, *Adv. Funct. Mater.* **2022**, *32*, 2111635.
[66] X. He, Y. Cui, Y. Qian, Y. Wu, H. Ling, H. Zhang, X.-Y. Kong, Y. Zhao, M. Xue, L. Jiang, L. Wen, *J. Am. Chem. Soc.* **2022**, *144*, 11168–11177.
[67] Y. Qin, H. Li, C. Han, F. Mo, X. Wang, *Adv. Mater.* **2022**, *34*, 2207118.

Entry for the Table of Contents

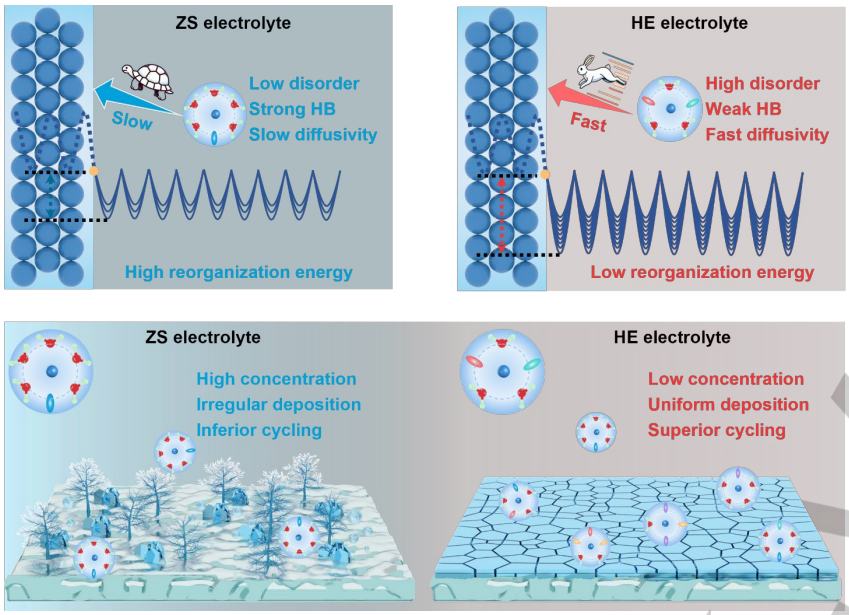

A novel low-concentration HE electrolyte is developed to address dendrite formation and side reactions in aqueous ZIBs. This HE electrolyte features weakly solvated structures and multiple anions, leading to highly disordered solvation shells that enhance zinc ion diffusion kinetics and electrode interface stability. As a result, Zn||Zn symmetric cells reach over 2,000 hours of cycling, and Zn||Cu cells achieve 99.9% CE over 1,000 cycles.